Supplementary material

Global scale variability of the mineral dust longwave refractive index: a new dataset of in situ measurements for climate modelling and remote sensing

Claudia Di Biagio[1], Paola Formenti[1], Yves Balkanski[2], Lorenzo Caponi[1,3], Mathieu Cazaunau[1], Edouard Pangui[1], Emilie Journet[1], Sophie Nowak[4], Sandrine Caquineau[5], Meinrat O. Andreae[6,12], Konrad Kandler[7], Thuraya Saeed[8], Stuart Piketh[9], David Seibert[10], Earle Williams[11], and Jean-François Doussin[1]

[1] *Laboratoire Interuniversitaire des Systèmes Atmosphériques (LISA), UMR 7583, CNRS, Université Paris Est Créteil et Université Paris Diderot, Institut Pierre et Simon Laplace, Créteil, France*

[2] *Laboratoire des Sciences du Climat et de l'Environnement, CEA CNRS UVSQ, 91191, Gif sur Yvette, France*

[3] *University of Genoa, Genoa, Italy*

[4] *Plateforme RX UFR de chimie, Université Paris Diderot, Paris, France*

[5] *IRD-Sorbonne Universités (UPMC, Univ. Paris 06) – CNRS-MNHN, LOCEAN Laboratory, IRD France-Nord, F-93143 Bondy, France*

[6] *Biogeochemistry Department, Max Planck Institute for Chemistry, P.O. Box 3060, 55020, Mainz, Germany*

[7] *Institut für Angewandte Geowissenschaften, Technische Universität Darmstadt, Schnittspahnstr. 9, 64287 Darmstadt, Germany*

[8] *Science department, College of Basic Education, Public Authority for Applied Education and Training, Al-Ardeya, Kuwait*

[9] *Climatology Research Group, Unit for Environmental Science and Management, North-West University, Potchefstroom, South Africa*

[10] *Walden University, Minneapolis, Minnesota, USA*

[11] *Parsons Laboratory, Massachusetts Institute of Technology, Cambridge, Massachusetts, USA*

[12] *Geology and Geophysics Department, King Saud University, Riyadh, Saudi Arabia*

Correspondence to:

C. Di Biagio (cldibiagio@gmail.com) and P. Formenti (paola.formenti@lisa.u-pec.fr)

Table S1. Calibration coefficients by mineral, obtained from the calibration of the diffractometer used in this study. The origin of the standard minerals is reported. The calibration coefficients (K_i) represent the slope of the linear fit between the number of diffracted counts by unit mass. The correlation coefficient R^2 of the fit for each mineral is also reported.

Mineral	**Origin**	**K_i (cps mg^{-1})**	**R^2**
Quartz	Fontainebleau, France	2874 ± 272	0.80
Orthoclase	Galerie des mineraux de Paris, France	2850 ± 389	0.69
Albite	Ontario, Canada	1271 ± 108	0.98
Calcite	Bédarieux, France	2288 ± 242	0.99
Dolomite	Traversella, Italy	2945 ± 276	0.99
Gypsum	Unknown	1053 ± 189	0.99

Table S2. Mineralogical composition (percentage by mass) of the nineteen dust samples analyzed in this study. The estimated uncertainties associated with the identification of the different mineral species are for clays ±14–100 %, quartz ±9 %, feldspars ±8–14 %, calcite ±11 %, dolomite ±10 %, gypsum ±18 %, and iron oxides (goethite and hematite) ±15 %. Values in parenthesis for clays represent the minimum and the maximum of the clay content calculated by using the M_{size} and $M_{elemental}$ estimates (as discussed in Sect. 2.4 in the paper).

Sample name	Clays	Quartz	Feldspars	Calcite	Dolomite	Gypsum	Goethite	Hematite
Tunisia	49.2% (0–66%)	18.4%	4.6%	23.3%	2.2%	ND	1.1%	1.2%
Morocco	63.2% (31–75%)	8.5%	2.1%	21.7%	3.1%	ND	1.0%	0.4%
Lybia	78.9% (70–84%)	12.1%	5.0%	0.9%	0.0%	ND	2.2%	0.9%
Algeria	63.5% (54–70%)	21.5%	7.9%	4.4%	0.0%	ND	1.4%	1.4%
Mauritania	90.4% (89–92%)	2.6%	2.3%	1.3%	0.0%	ND	0.0%	3.3%
Niger	51.2% (39–59%)	36.7%	6.3%	0.0%	0.0%	ND	3.5%	2.3%
Mali	59.8% (0–75%)	32.4%	4.1%	0.0%	0.0%	ND	1.7%	2.0%
Bodélé	53.5% (4–69%)	31.5%	14.3%	0.0%	0.0%	ND	0.0%	0.7%
Ethiopia	91.5% (88–93%)	2.5%	3.0%	1.0%	0.0%	ND	0.0%	2.0%
Saudi Arabia	71.6% (56–79%)	7.9%	2.6%	15.3%	0.0%	ND	0.8%	1.8%
Kuwait	56.7% (0–72%)	25.0%	14.8%	2.0%	0.0%	ND	0.0%	1.5%
Gobi	45.5% (33–54%)	27.0%	7.9%	18.7%	0.0%	ND	0.0%	0.9%
Taklimakan	66.2% (8–79%)	12.2%	8.1%	11.3%	2.2%	ND	0.0%	0.0%
Arizona	63.1% (32–75%)	18.9%	10.1%	6.4%	0.0%	ND	0.0%	1.5%
Atacama	69.4% (64–73%)	10.5%	6.1%	12.4%	0.0%	ND	0.0%	1.6%
Patagonia	51.2% (48–54%)	41.5%	5.8%	0.0%	0.0%	ND	0.6%	0.9%
Namib-1	75.6% (68–80%)	3.5%	5.6%	14.1%	0.0%	ND	0.3%	0.8%
Namib-2	86.2% (82–89%)	4.2%	3.5%	1.3%	0.0%	ND	0.0%	4.8%
Australia	56.7% (43–65%)	33.6%	6.1%	0.0%	0.0%	ND	0.0%	3.6%

ND = Not Detected

Figure S1. Upper panel: phase function of dust aerosols calculated for the Algeria case at the peak of the dust injection and 120 min after the peak at the wavelengths of 3, 6, 10, and 15 µm. Lower panel: calculated scattering-to-absorption ratio as a function of the wavelength as seen by the FTIR. Calculations have been performed by subtracting from the total integrated scattering the fraction towards the forward direction, which enters the FTIR detector and is not measured as extinction. The fraction that enters the FTIR has been calculated by taking into account the geometry of the instrument and the dust size, and it is larger than 50-70% at all wavelengths considered. Uncertainties in the scattering-to-absorption ratio are calculated with the error propagation formula taking into account the uncertainty in the size distribution. The obtained scattering-to-absorption ratio indicates that scattering is predominant at 3 µm, also mostly due to the fact that absorption is close to zero at this wavelength, whereas above 6 µm it represents on average less than 10% of the absorption signal. Thus, we can reasonably assume that above 6 µm the FTIR spectrum represents dust absorption.

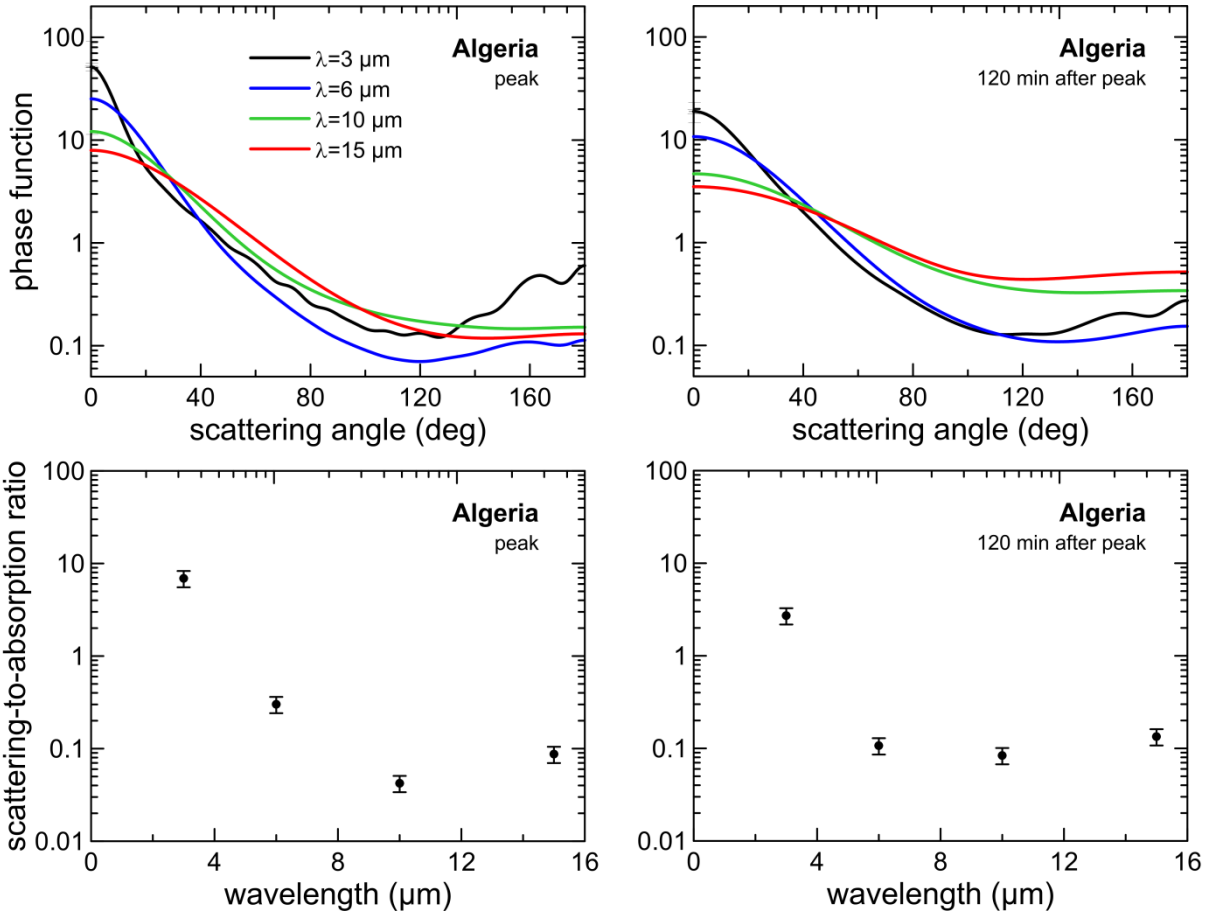

Figure S2. Emission spectrum of the WELAS white light source (Xenon arc lamp 35 W) measured with a LI-COR LI-1800.

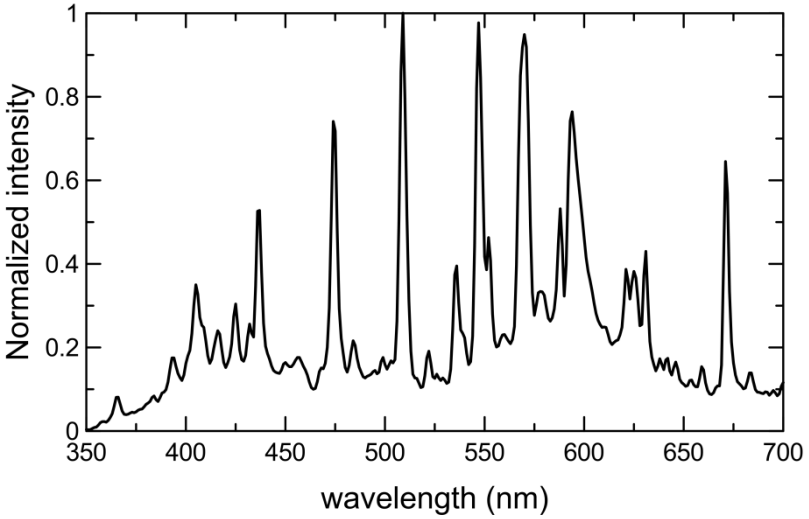

Figure S3. Comparison of the size distribution for the different instruments. Measurements from the SMPS (D_g=0.1-0.3 µm), the SkyGrimm (D_g=0.3-1.0 µm), and the WELAS (D_g>1.0 µm) at 30 min after the peak of the injection for the Algeria and Atacama cases are shown. Error bars indicate the 10-min standard deviation for the SMPS and the SkyGrimm, and the combination of standard deviation and L_{WELAS} (D_g) uncertainty for the WELAS. Error bars that extend to negative numbers on the log scale have been omitted for clarity. The interpolation curve at D_g>8 µm is also reported in the plot.

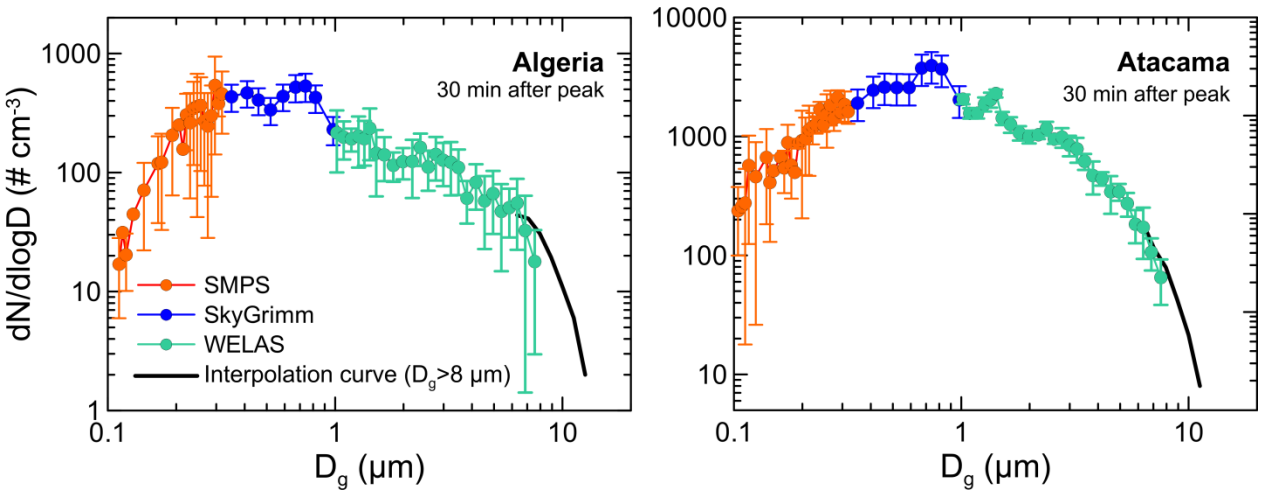

Figure S4. Comparison of the size distribution within the CESAM chamber (labelled as FTIR) and at the input of the sampling filter system measured at 30 min after the peak of the injection for the Algeria case.

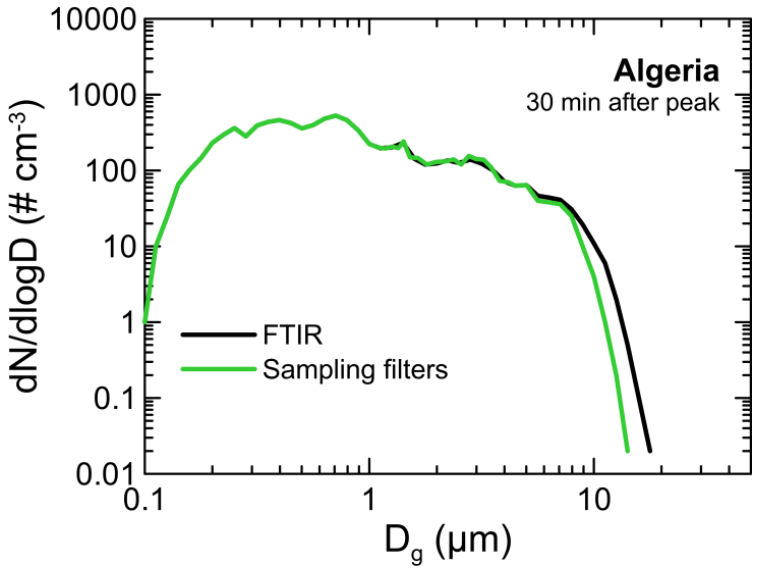

Figure S5. Number distribution ($dN/dlogD_g$, bottom panel), mass distribution ($dM/dlogD_g$ center panel), and total mass concentration (top panel) measured in CESAM during the experiment with Arizona dust.